Finite Difference Hermite WENO Schemes for Hyperbolic Conservation Laws

Hongxia Liu & Jianxian Qiu

Journal of
SCIENTIFIC
COMPUTING

Springer

Springer

Springer

Finite Difference Hermite WENO Schemes for Hyperbolic Conservation Laws

Hongxia Liu · Jianxian Qiu

Abstract In this paper, a class of weighted essentially non-oscillatory (WENO) schemes based on Hermite polynomials, termed HWENO (Hermite WENO) schemes, for solving one and two dimensional nonlinear hyperbolic conservation law systems is presented. The construction of HWENO schemes is based on a finite difference formulation, Hermite interpolation, and nonlinearly stable Runge–Kutta methods. The idea of the reconstruction in the HWENO schemes comes from the original WENO schemes, however both the function and its first derivative values are evolved in time and used in the reconstruction, while only the function values are evolved and used in the original WENO schemes. Comparing with the original finite difference WENO schemes of Jiang and Shu (J Comput Phys 126:202–228, 1996), one major advantage of HWENO schemes is its compactness in the reconstruction. For example, five points are needed in the stencil for a fifth order WENO (WENO5) reconstruction, while only three points are needed for a fifth order HWENO (HWENO5) reconstruction. Some benchmark numerical experiments are presented to illustrate efficiency of HWENO schemes.

H. Liu
School of Mathematical Sciences, Xiamen University, Xiamen 361005, Fujian,
People's Republic of China
e-mail: hx_ryu@163.com

J. Qiu (✉)
School of Mathematical Sciences, Fujian Provincial Key Laboratory of Mathematical Modeling and High-Performance Scientific Computation, Xiamen University, Xiamen, Fujian 361005,
People's Republic of China
e-mail: jxqiu@xmu.edu.cn

🌱 Springer

1 Introduction

In this paper, we investigated the finite difference Hermite weighted essentially non-oscillatory (HWENO) schemes for solving the nonlinear hyperbolic conservation laws:

$$\mathbf{u}_t + \nabla \cdot F(\mathbf{u}) = 0. \tag{1.1}$$

Hyperbolic conservation laws (1.1) and convection dominated PDEs play an important role arise in applications, such as gas dynamics, modeling of shallow waters. There are special difficulties associated with solving these problems both on mathematical and numerical methods, for discontinuous may appear in the solutions for nonlinear equations, even though the initial conditions are smooth enough. This is why devising robust, accurate and efficient methods for numerically solving these problems is of considerable importance and as expected, has attracted the interest of many researchers and practitioners. Within recent decades, many high-order numerical methods have been developed to solve these problem. Among them, we would like to mention essentially non-oscillatory (ENO) and weighted ENO (WENO) schemes, which have been applied quite successfully to solve the problems with shocks, contact discontinuities, and complicated smooth solutions.

In 1987, Harten et al. [2,3] introduced finite volume ENO schemes, which is a modification of total variation diminishing (TVD) scheme [1]. ENO schemes use an adaptive stencil based on the local smoothness such that it yields high-order accuracy where the function is smooth but avoids the Gibbs phenomena at discontinuities. In 1988 and 1989, Shu and Osher presented a class finite difference ENO schemes [11,12]. One of the popular high order numerical methods WENO scheme was proposed by Liu et al. [6], which is an improved version of the ENO technique using a cell-averaged approach for a third order finite volume version, in which it used a nonlinear convex combination of all the candidate stencils to improve the accuracy of numerical fluxes without destroying non-oscillatory behaviors near discontinuities, while additionally obtaining one order of improvement in accuracy. In 1996, third and fifth order finite difference WENO schemes in multi space dimensions are constructed by Jiang and Shu [5], with a general framework for the design of smoothness indicators and nonlinear weights. Instead of using just one candidate stencil, a linear combination of all candidate stencils is used. A key idea in WENO schemes is a linear combination of lower order fluxes or reconstruction to obtain a higher order approximation. ENO and WENO schemes have following advantages: uniform high order accuracy in smooth regions including at smooth extreme, unlike second order TVD schemes which degenerate to first order accuracy at smooth extreme; sharp and ENO (to the eyes) shock transition; robust for many physical systems with strong shocks and especially suitable for simulating solutions containing both discontinuities and complicated smooth solution structure, such as shock interaction with vortices.

In 2004, following the idea of WENO, Qiu and Shu presented a class of Hermite WENO (HWENO) schemes [7] in which both the function and its first derivative values are evolved in time and used in the reconstruction, while only the function values are evolved and used in the original WENO schemes. The construction of HWENO schemes were based on a *finite volume* formulation, and they were applied as the limiters for the Runge–Kutta discontinuous Galerkin (RKDG) methods [7,8]. Then HWENO schemes were extended to solve two-dimensional conservation laws in [8,16] and Hamilton-Jacobi equations in [9]. In this paper, we presented the fifth order finite difference Hermite WENO (HWENO). The construction of HWENO schemes is based on a finite difference formulation, Hermite interpolation, and nonlinearly stable Runge–Kutta methods. Comparing with the original finite difference WENO schemes of Jiang and Shu [5], one major advantage of HWENO schemes is its

compactness in the reconstruction. For example, five points are needed in the stencil for a fifth order WENO (WENO5) reconstruction, while only three points are needed for a fifth order HWENO (HWENO5) reconstruction.

The organization of this paper is as follows: In Sect. 2, we will describe the reconstruction procedure of finite difference HWENO schemes in one-dimensional cases. In Sect. 3, we extended the method to two-dimensional cases and a practicable method for the hybrid derivative terms is discussed. A number of typical numerical examples is provided to demonstrate the behavior of the HWENO schemes in Sect. 4. Concluding remarks are given in Sect. 5.

2 Description of HWENO Scheme in One Dimensional Case

In this section, we concentrate on describing the fifth-order finite difference HWENO schemes for hyperbolic conservation laws (1.1). At first, we describe the reconstruction procedure of finite difference HWENO schemes in one-dimensional scalar cases. Consider the one-dimensional scalar conservation laws of (1.1):

$$\begin{cases} u_t + f(u)_x = 0, & x \in (-\infty, \infty), \ t \in (0, \infty) \\ u(x, 0) = u_0(x), & x \in (-\infty, \infty) \end{cases} \tag{2.1}$$

where $u(x, t)$ is a conserved quantity, $f(u(x, t))$ is flux, and x and t denote space and time variable, respectively. We consider an uniform grid defined by the points $x_i = \frac{1}{2}(x_{i-\frac{1}{2}} + x_{i+\frac{1}{2}})$, $i = 1, \ldots, N$, which are also called cell centers, with cell boundaries given by $x_{i+\frac{1}{2}} = x_i + \frac{1}{2}\Delta x$, where $\Delta x = x_{i+\frac{1}{2}} - x_{i-\frac{1}{2}}$ is the uniform grid spacing, the cells denoted by $I_i = [x_{i-\frac{1}{2}}, x_{i+\frac{1}{2}}]$. Denote the derivative of function $u(x)$ as $v(x)$, then from (2.1) and its spatial derivative, we have the following equations:

$$\begin{cases} u_t + f(u)_x = 0, & u(x, 0) = u_0(x), \\ v_t + h(u, v)_x = 0, & v(x, 0) = v_0(x), \end{cases} \tag{2.2}$$

where $h(u, v) = f(u)_x = f'(u)u_x = f'(u)v$. A conservative numerical scheme ensures that a quantity remains conserved by calculating a single flux which describes the flow of that quantity between neighboring cells. One solves (2.2) directly using a semi-discrete conservative approximation to the spatial derivatives by the finite differences:

$$\begin{cases} \frac{du_i(t)}{dt} = -\frac{1}{\Delta x}(\hat{f}_{i+\frac{1}{2}} - \hat{f}_{i-1/2}), \\ \frac{dv_i(t)}{dt} = -\frac{1}{\Delta x}(\hat{h}_{i+\frac{1}{2}} - \hat{h}_{i-1/2}), \end{cases} \tag{2.3}$$

where $u_i(t)$ and $v_i(t)$ are the numerical approximation to the point value $u(x_i, t)$ and $v(x_i, t)$, and the numerical flux

$$\begin{aligned} \hat{f}_{i+\frac{1}{2}} &= \hat{f}(u_{i-r}, \ldots, u_{i+s}, v_{i-r}, \ldots, v_{i+s}), \\ \hat{h}_{i+\frac{1}{2}} &= \hat{h}(u_{i-r}, \ldots, u_{i+s}, v_{i-r}, \ldots, v_{i+s}) \end{aligned} \tag{2.4}$$

satisfies the usual conditions, such as $\hat{f}_{i+\frac{1}{2}}$ and $\hat{h}_{i+\frac{1}{2}}$ are all Lipschitz continuous functions with respect to all its arguments, $\hat{f}_{i+\frac{1}{2}}$ and $\hat{h}_{i+\frac{1}{2}}$ are consistent with the physical flux $\hat{f}(u, \ldots, u, v, \ldots, v) = f(u)$ and $\hat{h}(u, \ldots, u, v, \ldots, v) = h(u, v)$.

The scheme (2.3) has the rth order accuracy if

$$\begin{cases} \frac{1}{\Delta x}\big(\hat{f}_{i+\frac{1}{2}} - \hat{f}_{i-\frac{1}{2}}\big) = f(u)_x|_{x=x_i} + O(\Delta x^r), \\ \frac{1}{\Delta x}\big(\hat{h}_{i+\frac{1}{2}} - \hat{h}_{i-\frac{1}{2}}\big) = h(u,v)_x|_{x=x_i} + O\big(\Delta x^{r-1}\big), \end{cases} \tag{2.5}$$

when u, v is smooth in the stencil.

Following [5], we define the implicit functions $\varphi(x)$ and $\psi(x)$, such that

$$\frac{1}{\Delta x}\int_{x-\frac{\Delta x}{2}}^{x+\frac{\Delta x}{2}} \varphi(\xi)d\xi = f(u(x)), \quad \frac{1}{\Delta x}\int_{x-\frac{\Delta x}{2}}^{x+\frac{\Delta x}{2}} \psi(\eta)d\eta = h(u(x), v(x)), \tag{2.6}$$

then we have:

$$\begin{cases} \frac{1}{\Delta x}(\varphi(x_{i+\frac{1}{2}}) - \varphi(x_{i-\frac{1}{2}})) = f(u)_x|_{x=x_i}, \\ \frac{1}{\Delta x}(\psi(x_{i+\frac{1}{2}}) - \psi(x_{i-\frac{1}{2}})) = h(u,v)_x|_{x=x_i}. \end{cases} \tag{2.7}$$

If we choose numerical fluxes $\hat{f}_{i+\frac{1}{2}}$ and $\hat{h}_{i+\frac{1}{2}}$ such that

$$\begin{cases} \hat{f}_{i+\frac{1}{2}} = \varphi(x_{i+\frac{1}{2}}) + O(\Delta x^r), \\ \hat{h}_{i+\frac{1}{2}} = \psi(x_{i+\frac{1}{2}}) + O(\Delta x^{r-1}), \end{cases} \tag{2.8}$$

then the scheme (2.3) has the rth order accuracy.

The definition of $\varphi(x)$ and $\psi(x)$ (2.6) implies that

$$\bar{\varphi}_i = \frac{1}{\Delta x}\int_{x_{i-\frac{1}{2}}}^{x_{i+\frac{1}{2}}} \varphi(\xi)d\xi = f(u_i), \quad \bar{\psi}_i = \frac{1}{\Delta x}\int_{x_{i-\frac{1}{2}}}^{x_{i+\frac{1}{2}}} \psi(\eta)d\eta = h(u_i, v_i). \tag{2.9}$$

Using the conditions (2.9), we can reconstruct fluxes $\hat{f}_{i+\frac{1}{2}}$ and $\hat{h}_{i+\frac{1}{2}}$ which satisfy (2.8).

For the purpose of stability, we need consider the upwind quality of the schemes. We will split fluxes $f(u)$ and $h(u,v)$ into two parts, respectively, $f(u) = f^+(u) + f^-(u)$ and $h(u,v) = h^+(u,v) + h^-(u,v)$, where $\frac{d}{du}f^+(u) \geq 0, \frac{\partial}{\partial v}h^+(u,v) \geq 0, \frac{d}{du}f^-(u) \leq 0, \frac{\partial}{\partial v}h^-(u,v) \leq 0$. The reconstruction procedure which will be described below for numerical fluxes $\hat{f}_{i+\frac{1}{2}}$ and $\hat{h}_{i+\frac{1}{2}}$ will also be split into two parts and be applied to $f^+(u), h^+(u,v)$ and $f^-(u), h^-(u,v)$, respectively. Hence, numerical fluxes

$$\hat{f}_{i+\frac{1}{2}} = \hat{f}^+_{i+\frac{1}{2}} + \hat{f}^-_{i+\frac{1}{2}}, \quad \hat{h}_{i+\frac{1}{2}} = \hat{h}^+_{i+\frac{1}{2}} + \hat{h}^-_{i+\frac{1}{2}}. \tag{2.10}$$

Then the semi-discrete scheme (2.3), written as an ordinary differential equation (ODE) system

$$U_t = L(U) \tag{2.11}$$

is then discretized in time by a total variation diminishing (TVD) Runge–Kutta method [11,12], for example the third order version given by

$$\begin{aligned} U^{(1)} &= U^n + \Delta t L(U^n) \\ U^{(2)} &= \frac{3}{4}U^n + \frac{1}{4}U^{(1)} + \frac{1}{4}\Delta t L(U^{(1)}) \\ U^{n+1} &= \frac{1}{3}U^n + \frac{2}{3}U^{(2)} + \frac{2}{3}\Delta t L(U^{(2)}), \end{aligned} \tag{2.12}$$

with $U = (u, v)^T$.

Now we describe the procedure of HWENO reconstruction for numerical fluxes in detail.

Step 1. We first consider the reconstruction of $\hat{f}_{i+\frac{1}{2}}$, the procedure of the algorithm is as below.

1.1. Given the nodal value $\{u_i, v_i\}$, we can use the following splitting procedure to get $\{f^\pm(u_i), h^\pm(u_i, v_i)\}$:

$$f^+(u_i) = \tfrac{1}{2}(f(u_i) + \alpha u_i), \quad f^-(u_i) = \tfrac{1}{2}(f(u_i) - \alpha u_i);$$
$$h^+(u_i, v_i) = \tfrac{1}{2}(h(u_i, v_i) + \alpha v_i), \quad h^-(u_i, v_i) = \tfrac{1}{2}(h(u_i, v_i) - \alpha v_i), \tag{2.13}$$

with the $\alpha = \max_u |f'(u)|$.

1.2. Given the small stencils $s_0 = \{x_{i-1}, x_i\}$, $s_1 = \{x_i, x_{i+1}\}$, $s_2 = \{x_{i-1}, x_i, x_{i+1}\}$ and the bigger stencil $\mathcal{T} = s_0 \cup s_1 \cup s_2$, we construct quadratic polynomials $p_0(x), p_1(x), p_2(x)$ and a fourth-degree reconstruction polynomial $q(x)$ such that:

$$\frac{1}{\Delta x}\int_{I_k} p_0(x)dx = f^+(u_k), \quad k = i-1, i,$$

$$\frac{1}{\Delta x}\int_{I_{i-1}} p_0'(x)dx = h^+(u_{i-1}, v_{i-1});$$

$$\frac{1}{\Delta x}\int_{I_k} p_1(x)dx = f^+(u_k), \quad k = i, i+1,$$

$$\frac{1}{\Delta x}\int_{I_{i+1}} p_1'(x)dx = h^+(u_{i+1}, v_{i+1});$$

$$\frac{1}{\Delta x}\int_{I_k} p_2(x)dx = f^+(u_k), \quad k = i-1, i, i+1;$$

and

$$\frac{1}{\Delta x}\int_{I_k} q(x)dx = f^+(u_k), \quad k = i-1, i, i+1,$$

$$\frac{1}{\Delta x}\int_{I_k} q'(x)dx = h^+(u_k, v_k), \quad k = i-1, i+1.$$

Notice that we follow the principle of unilateral choice of derivative condition in order to consider stability of numerical schemes. We would like to find an approximation of function $p_j(x)$ and $q(x)$ at the half nodes $x_{i+\frac{1}{2}}$, hence, we have

$$p_0\left(x_{i+\frac{1}{2}}\right) = -\frac{7}{6}f^+(u_{i-1}) + \frac{13}{6}f^+(u_i) - \frac{2}{3}\Delta x h^+(u_{i-1}, v_{i-1}),$$

$$p_1\left(x_{i+\frac{1}{2}}\right) = \frac{1}{6}f^+(u_i) + \frac{5}{6}f^+(u_{i+1}) - \frac{1}{3}\Delta x h^+(u_{i+1}, v_{i+1}),$$

$$p_2\left(x_{i+\frac{1}{2}}\right) = -\frac{1}{6}f^+(u_{i-1}) + \frac{5}{6}f^+(u_i) + \frac{1}{3}f^+(u_{i+1}), \tag{2.14}$$

$$q\left(x_{i+\frac{1}{2}}\right) = -\frac{23}{120}f^+(u_{i-1}) + \frac{19}{30}f^+(u_i)$$
$$+ \frac{67}{120}f^+(u_{i+1}) - \Delta x\left(\frac{3}{40}h^+(u_{i-1}, v_{i-1})\right.$$
$$\left. + \frac{7}{40}h^+(u_{i+1}, v_{i+1})\right).$$

1.3. A crucial component for HWENO procedure is to write the $q(x)$ as linear convex combination of polynomial $p_0(x)$, $p_1(x)$, $p_2(x)$ at $x = x_{i+\frac{1}{2}}$. Simple algebra gives the combination coefficients $\gamma_j (j = 0, 1, 2)$, also called linear weights, satisfying:

$$q(x_{i+\frac{1}{2}}) = \sum_{j=0}^{2} \gamma_j p_j \left(x_{i+\frac{1}{2}}\right)$$

with $\sum_{j=0}^{2} \gamma_j = 1$ for all the nodal values of f^+ and h^+ in the bigger stencil $\mathcal{T}$. This leads to

$$\gamma_0 = \frac{9}{80}, \ \gamma_1 = \frac{42}{80}, \ \gamma_2 = \frac{29}{80}. \tag{2.15}$$

1.4. We compute the smoothness indicator, denoted by β_j for stencil s_j, which measures the smoothness of the function $p_j(x)$ in the target cell I_i. The smaller the value of β_j, the smoother the function $p_j(x)$ in its target cell. Moreover, smoothness indicator is the key component changing the linear weights obtained in the step 3 to nonlinear weights. We take the same form smoothness indicator as in [7]

$$\beta_j = \sum_{l=1}^{2} \int_{I_i} \Delta x^{2l-1} \left(\frac{\partial^l}{\partial x^l} p_j(x)\right)^2 dx. \tag{2.16}$$

In fact, it's an quadratic function of the values of the u and v in each stencil s_j. In this work, the smoothness indicator expressions are

$$\beta_0 = (-2f^+(u_{i-1}) + 2f^+(u_i) - \Delta x h^+(u_{i-1}, v_{i-1}))^2$$
$$+ \frac{13}{12}(-2f^+(u_{i-1}) + 2f^+(u_i) - 2\Delta x h^+(u_{i-1}, v_{i-1}))^2,$$
$$\beta_1 = (-2f^+(u_i) + 2f^+(u_{i+1}) - \Delta x h^+(u_{i+1}, v_{i+1}))^2$$
$$+ \frac{13}{12}(2f^+(u_i) - 2f^+(u_{i+1}) + 2\Delta x h^+(u_{i+1}, v_{i+1}))^2,$$
$$\beta_2 = \frac{1}{4}(-f^+(u_{i-1}) + f^+(u_{i+1}))^2$$
$$+ \frac{13}{12}(f^+(u_{i-1}) - 2f^+(u_i) + f^+(u_{i+1}))^2.$$

1.5. We compute the nonlinear weights w_j by

$$w_j = \frac{\bar{w}_j}{\sum_k \bar{w}_k}, \ \bar{w}_k = \frac{\gamma_k}{(\beta_k + \varepsilon)^2}, \ j, k = 0, 1, 2, \tag{2.17}$$

where γ_k are determined by (2.15), and the parameter ε is a positive real number which is introduced to avoid the denominator to be zero, ε is taken as 10^{-6} in all our numerical results. For more details one can see [5]. Then, the HWENO reconstruction approximation

$$\varphi_{i+\frac{1}{2}}^+ \approx \hat{f}_{i+\frac{1}{2}}^+ = \sum_{j=0}^{2} \omega_j p_j \left(x_{i+\frac{1}{2}}\right). \tag{2.18}$$

The reconstruction procedure of $\hat{f}^-_{i+\frac{1}{2}}$ from $\{f^-(u_i),\ h^-(u_i, v_i)\}$ is mirror symmetric with respect to $x_{i+\frac{1}{2}}$ of that for $\hat{f}^+_{i+\frac{1}{2}}$ described above.

1.6. Finally, our numerical flux can be obtained by

$$\hat{f}_{i+\frac{1}{2}} = \hat{f}^+_{i+\frac{1}{2}} + \hat{f}^-_{i+\frac{1}{2}}. \tag{2.19}$$

Step 2. The reconstruction of numerical flux $\hat{h}_{i+\frac{1}{2}}$.

2.1. Compute $\{f^\pm(u_i),\ h^\pm(u_i, v_i)\}$ as in Step 1.1.

2.2. Given the small stencils $s_0 = \{x_{i-1}, x_i\}$, $s_1 = \{x_i, x_{i+1}\}$, $s_2 = \{x_{i-1}, x_i, x_{i+1}\}$ and the big stencil $\mathcal{T} = s_0 \cup s_1 \cup s_2$, we construct Hermite cubic reconstruction polynomials $p_0(x)$, $p_1(x)$, $p_2(x)$ and a fifth-degree reconstruction polynomial $q(x)$ such that:

$$\frac{1}{\Delta x} \int_{I_k} p_0(x)dx = f^+(u_k), \quad \frac{1}{\Delta x} \int_{I_k} p_0'(x)dx = h^+(u_k, v_k), \quad k = i-1, i;$$

$$\frac{1}{\Delta x} \int_{I_k} p_1(x)dx = f^+(u_k), \quad \frac{1}{\Delta x} \int_{I_k} p_1'(x)dx = h^+(u_k, v_k), \quad k = i, i+1;$$

$$\frac{1}{\Delta x} \int_{I_k} p_2(x)dx = f^+(u_k), \quad k = i-1, i, i+1; \quad \frac{1}{\Delta x} \int_{I_i} p_2'(x)dx = h^+(u_i, v_i)$$

and

$$\frac{1}{\Delta x} \int_{I_k} q(x)dx = f^+(u_k), \quad \frac{1}{\Delta x} \int_{I_k} q'(x)dx = h^+(u_k, v_k), \quad k = i-1, i, i+1.$$

Find an approximation of function $p_j'(x)$ and $q'(x)$ at the half nodes $x_{i+\frac{1}{2}}$, hence, we can have

$$p_0'(x_{i+\frac{1}{2}}) = \frac{4}{\Delta x}(f^+(u_{i-1}) - f^+(u_i)) + \frac{3}{2}h^+(u_{i-1}, v_{i-1}) + \frac{7}{2}h^+(u_i, v_i),$$

$$p_1'(x_{i+\frac{1}{2}}) = -\frac{2}{\Delta x}(f^+(u_i) - f^+(u_{i+1})) - \frac{1}{2}h^+(u_i, v_i) - \frac{1}{2}h^+(u_{i+1}, v_{i+1}),$$

$$p_2'(x_{i+\frac{1}{2}}) = \frac{1}{4\Delta x}(f^+(u_{i-1}) - 4f^+(u_i) + 3f^+(u_{i+1})) + \frac{1}{2}h^+(u_i, v_i),$$

$$q'(x_{i+\frac{1}{2}}) = \frac{1}{\Delta x}(\frac{1}{4}f^+(u_{i-1}) - 2f^+(u_i) + \frac{7}{4}f^+(u_{i+1}))$$
$$+ \frac{1}{12}h^+(u_{i-1}, v_{i-1}) - \frac{1}{6}h^+(u_i, v_i) - \frac{5}{12}h^+(u_{i+1}, v_{i+1}). \tag{2.20}$$

2.3. Similarly, compute the linear weights γ_j', $j = 1, 2, 3$, such that

$$q'\left(x_{i+\frac{1}{2}}\right) = \sum_{j=0}^{2} \gamma_j' p_j'\left(x_{i+\frac{1}{2}}\right),$$

with $\sum_{j=0}^{2} \gamma_j' = 1$, for all the nodal values of f^+ and h^+ in the bigger stencil $\mathcal{T}$. This leads to

$$\gamma_0' = \frac{1}{18}, \quad \gamma_1' = \frac{5}{6}, \quad \gamma_2' = \frac{1}{9}. \tag{2.21}$$

2.4. Again we define the smoothness indicators for the reconstruction of derivatives as

$$\beta_j = \sum_{l=2}^{3} \int_{I_i} \Delta x^{2l-1} \left(\frac{\partial^l}{\partial x^l} p_j(x) \right)^2 dx. \tag{2.22}$$

Then we can express the smoothness indicator explicitly a quadratic function forms as follows

$$\beta_0 = \frac{13}{3}(6f^+(u_{i-1}) - 6f^+(u_i) + 3\Delta x(h^+(u_{i-1}, v_{i-1}) + h^+(u_i, v_i)))^2$$
$$+ (6f^+(u_{i-1}) - 6f^+(u_i) + 2\Delta x(h^+(u_{i-1}, v_{i-1}) + 2h^+(u_i, v_i)))^2,$$
$$\beta_1 = \frac{13}{3}(6f^+(u_i) - 6f^+(u_{i+1}) + 3\Delta x(h^+(u_i, v_i) + h^+(u_{i+1}, v_{i+1})))^2$$
$$+ (-6f^+(u_i) + 6f^+(u_{i+1}) - 2\Delta x(2h^+(u_i, v_i) + h^+(u_{i+1}, v_{i+1})))^2,$$
$$\beta_2 = \frac{13}{12}(-3f^+(u_{i-1}) + 3f^+(u_{i+1}) - 6\Delta x h^+(u_i, v_i))^2$$
$$+ (f^+(u_{i-1}) - 2f^+(u_i) + f^+(u_{i+1}))^2.$$

2.5. Compute the nonlinear weights based on the smoothness indicators in step 2.4, we have

$$w'_j = \frac{\bar{w}'_j}{\sum_k \bar{w}'_k}, \quad \bar{w}'_k = \frac{\gamma'_k}{(\beta_k + \varepsilon)^2}, \quad j, k = 0, 1, 2, \tag{2.23}$$

where γ'_k are the weights determined by (2.21), and the parameter ε is again a positive real number to avoid the denominator to be zero, ε is taken as 10^{-6} in all our numerical results. Then, the HWENO reconstruction approximation

$$\varphi^+_{i+\frac{1}{2}} \approx \hat{h}^+_{i+\frac{1}{2}} = \sum_{j=0}^{2} \omega'_j p'_j \left(x_{i+\frac{1}{2}} \right). \tag{2.24}$$

Again, the reconstruction procedure of $\hat{h}^-_{i+\frac{1}{2}}$ from $\{f^-(u_i), h^-(u_i, v_i)\}$ is mirror symmetric with respect to $x_{i+\frac{1}{2}}$ of that for $\hat{h}^+_{i+\frac{1}{2}}$ described above.

2.6. Finally, our numerical flux can be obtained by

$$\hat{h}_{i+\frac{1}{2}} = \hat{h}^+_{i+\frac{1}{2}} + \hat{h}^-_{i+\frac{1}{2}} \tag{2.25}$$

Remark 1 For systems of conservation laws, the procedure of reconstruction of numerical fluxes are performed in the local characteristic directions to avoid oscillation.

Remark 2 Positivity-preserving flux limiter is key point for high-order numerical methods, which is used to maintain the density ρ and the pressure p to be positive. There are serval positivity-preserving methods in the literature, such as [4,14,15]. In this paper we take the technique by Hu et al. [4], for details refer to [4].

3 Description of HWENO Scheme in Two Dimensional Case

In this section we extend the method in Sect. 2 to solve nonlinear hyperbolic conservation laws. Firstly we consider 2D scalar conservation laws

$$\begin{cases} u_t + f(u)_x + g(u)_y = 0, & (x, y) \in R^2, \ t \in (0, \infty) \\ u(x, y, 0) = u_0(x, y), & (x, y) \in R^2, \end{cases} \tag{3.1}$$

where $u(x, y, t)$ is a conserved quantity, $f(u(x, y, t))$ and $g(u(x, y, t))$ describes its flux in x direction and y direction. Let $v = u_x$, $w = u_y$, taking the derivative x and y of (3.1) separately, then we obtain the whole equations form that we need to solve as below

$$\begin{cases} u_t + f(u)_x + g(u)_y = 0, \\ v_t + h(u, v)_x + r(u, v)_y = 0, \\ w_t + q(u, w)_x + s(u, w)_y = 0, \end{cases} \tag{3.2}$$

where

$$h(u, v) = f'(u)v, \ r(u, v) = g'(u)v,$$
$$q(u, w) = f'(u)w, \ s(u, w) = g'(u)w.$$

In this section, the domain $[a, b] \times [c, d]$ is divided as $a = x_{\frac{1}{2}} < x_{\frac{3}{2}} \ldots < x_{N_x+\frac{1}{2}} = b$, $c = y_{\frac{1}{2}} < y_{\frac{3}{2}} \ldots < y_{N_y+\frac{1}{2}} = d$ with uniformly distributed grid points, i.e. $x_i = a + i \Delta x$, $y_j = c + j \Delta y$. We define the cell size $x_{i+\frac{1}{2}} - x_{i-1/2} = \Delta x$, $y_{j+1/2} - y_{j-1/2} = \Delta y$, and cell centers $(x_i, y_j) = (\frac{1}{2}(x_{i+\frac{1}{2}} + x_{i-1/2}), \frac{1}{2}(y_{j+1/2} - y_{j-1/2}))$. Note that the components in both Eqs. (3.2) and (2.2) have the similar form, we can extend the algorithm for one dimensional case in a dimension-by-dimension fashion to two dimensional case. But it is difficult to approximate the mixed derivative terms $(f'(u)w)_x$ and $(g'(u)v)_y$ with the same order of accuracy. The key point is how to reconstruct the numerical fluxes for the mixed derivative terms. In this paper the conventional 3-point WENO reconstruction is employed in mixed derivative terms, therefore the accuracy of two dimensional scheme is fourth order.

Again we approximate (3.2) by the following conservative schemes

$$\begin{cases} \frac{du_{i,j}(t)}{dt} + \frac{1}{\Delta x}(\hat{f}_{i+\frac{1}{2},j} - \hat{f}_{i-\frac{1}{2},j}) + \frac{1}{\Delta y}(\hat{g}_{i,j+\frac{1}{2}} - \hat{g}_{i,j-\frac{1}{2}}) = 0, \\ \frac{dv_{i,j}(t)}{dt} + \frac{1}{\Delta x}(\hat{h}_{i+\frac{1}{2},j} - \hat{h}_{i-\frac{1}{2},j}) + \frac{1}{\Delta y}(\hat{r}_{i,j+\frac{1}{2}} - \hat{r}_{i,j-\frac{1}{2}}) = 0, \\ \frac{dw_{i,j}(t)}{dt} + \frac{1}{\Delta x}(\hat{q}_{i+\frac{1}{2},j} - \hat{q}_{i-\frac{1}{2},j}) + \frac{1}{\Delta y}(\hat{s}_{i,j+\frac{1}{2}} - \hat{s}_{i,j-\frac{1}{2}}) = 0, \end{cases} \tag{3.3}$$

where the numerical fluxes $\hat{f}_{i+\frac{1}{2},j}$, $\hat{h}_{i+\frac{1}{2},j}$, $\hat{g}_{i,j+\frac{1}{2}}$, and $\hat{s}_{i,j+\frac{1}{2}}$, were reconstructed by the straightforward extended from the one dimensional methods in a dimension-by-dimension fashion.

For the reconstruction of the numerical fluxes $\hat{q}_{i+\frac{1}{2},j}$ for the mixed derivative terms q_x, we would like to adopt the following WENO procedure.

1. For any fixed $y = y_j$, we split the fluxes into positive and negative parts by:

$$q_{i,j}^+ = \frac{1}{2}(q(u_{i,j}, w_{i,j}) + \alpha w_{i,j}),$$
$$q_{i,j}^- = \frac{1}{2}(q(u_{i+1,j}, w_{i+1,j}) - \alpha w_{i+1,j}),$$

where $q(u_{i,j}, w_{i,j}) = q_{i,j} = f'(u_{i,j})w_{i,j}$, and $\alpha = \max_u |f'(u)|$.

2. Reconstruction the approximation using the WENO procedure. We choose the small stencils $s_1 = \{x_{i-1}, x_i\}$, $s_2 = \{x_i, x_{i+1}\}$ and a big stencil $\mathcal{T} = \{x_{i-1}, x_i, x_{i+1}\}$ at $y = y_j$. We interpolate linear polynomials $p_1(x)$, $p_2(x)$, satisfying

$$\frac{1}{\Delta x} \int_{I_k} p_1(x)dx = q_{k,j}^+ \ (k = i - 1, i), \quad \frac{1}{\Delta x} \int_{I_k} p_2(x)dx = q_{k,j}^+ \ (k = i, i + 1),$$

(3.4)

and $Q(x)$ in big stencil such that:

$$\frac{1}{\Delta x} \int_{I_k} Q(x)dx = q_{k,j}^+ (k = i - 1, i, i + 1).$$

A simple algebra leads to these polynomials at the cell boundaries $x = x_{i+1/2}$:

$$p_1\left(x_{i+\frac{1}{2}}^-\right) = -\frac{1}{2}q_{i-1,j}^+ + \frac{3}{2}q_{i,j}^+,$$

$$p_2\left(x_{i+\frac{1}{2}}^-\right) = \frac{1}{2}q_{i,j}^+ + \frac{1}{2}q_{i+1,j}^+.$$

and

$$Q\left(x_{i+\frac{1}{2}}^-\right) = -\frac{1}{6}q_{i-1,j}^+ + \frac{5}{6}q_{i,j}^+ + \frac{1}{3}q_{i+1,j}^+.$$

3. The approximation $Q(x_{i+\frac{1}{2},j}^-)$ can be written as a linear convex combination of the two second order approximations $p_1(x_{i+\frac{1}{2},j}^-)$ and $p_2(x_{i+\frac{1}{2},j}^-)$, defined in the above step. Denoting the linear weights by γ_1, γ_2 such that

$$Q\left(x_{i+\frac{1}{2}}^-\right) = \gamma_1 p_1\left(x_{i+\frac{1}{2}}^-\right) + \gamma_2 p_2\left(x_{i+\frac{1}{2}}^-\right).$$

where the constants γ_1, γ_2 satisfying $\gamma_1 + \gamma_2 = 1$. And here the linear weights are given as $\gamma_1 = \frac{1}{3}, \gamma_2 = \frac{2}{3}$.

4. Finally, we change the linear weights obtained in the third step to nonlinear weights. This is achieved through a choice of the so-called smoothness indicator $\beta_j (j = 1, 2)$. In this paper, we use the same formula with (2.16) obtaining the smoothness indicator expressions are

$$\beta_1 = (q_{i-1,j}^+ - q_{i,j}^+)^2, \quad \beta_2 = (-q_{i,j}^+ + q_{i+1,j}^+)^2.$$

The linear weights γ_j in the third step is then replaced by the nonlinear weights ω_j, defined by

$$\omega_j = \frac{\bar{\omega}_j}{\bar{\omega}_1 + \bar{\omega}_2}, \quad \bar{\omega}_j = \frac{\gamma_j}{(\varepsilon + \beta_j)^2}, \ j = 1, 2;$$

where ε is a small positive number to avoid the denominator to become zero. Then the approximation of $q_{i+\frac{1}{2},j}^+$ is achieved as

$$\hat{q}_{i+\frac{1}{2},j}^+ = \omega_1 p_1\left(x_{i+\frac{1}{2}}^-\right) + \omega_2 p_2\left(x_{i+\frac{1}{2}}^-\right).$$

5. Again, the reconstruction procedure of $\hat{q}^-_{i+\frac{1}{2},j}$, from $q^-_{i,j}$ is mirror symmetric with respect to $x_{i+\frac{1}{2}}$ of that for $\hat{q}^+_{i+\frac{1}{2},j}$ described above. Finally, we obtain numerical fluxes $\hat{q}_{i+\frac{1}{2},j}$ as:

$$\hat{q}_{i+\frac{1}{2},j} = \hat{q}^-_{i+\frac{1}{2},j} + \hat{q}^+_{i+\frac{1}{2},j}.$$

Notice that again for systems of conservation laws, such as the Euler equations of gas dynamics, all of the reconstructions are performed in the local characteristic directions of $f'(u)$ to avoid spurious oscillatory.

An analogous procedure is performed to the mixed derivative term $\hat{r}_{i,j\pm\frac{1}{2}}$ in the y-direction, and for systems case, all of the reconstructions are performed in the local characteristic directions of $g'(u)$.

Remark 3 The disadvantage of using this method to treat the mixed derivatives is that the scheme is only the forth order of accuracy.

Remark 4 If we use following linear finite difference to approximate mixed derivatives:

$$\hat{q}_{i+\frac{1}{2},j} = \frac{1}{12\Delta x}(-q_{i-1,j} + 7q_{i,j} + 7q_{i+1,j} - q_{i+2,j}),$$

then the scheme is the fifth order of accuracy, but when we use it to simulate the problem with strong discontinuity, spurious oscillatory will appear.

4 Numerical Results

In this section we perform a number of typical numerical experiments to test the performances of finite difference HWENO schemes. For all the numerical tests in this paper, the third order Runge–Kutta method (2.12) is used for time evolution, and *CFL* number is taken to be 0.2 for one and two dimensional cases, except for the accuracy tests where a suitably reduced time step is used to guarantee that spatial error dominates.

4.1 Scalar Conservation Laws in One Dimension

Example 4.1 The linear advection problem. We consider the linear advection equation:

$$\begin{cases} u_t + u_x = 0, & -1 \le x < 1, t > 0, \\ u(x, 0) = u_0(x). \end{cases} \tag{4.1}$$

The exact solution of this problem is $u(x, t) = u_0(x - t)$.

First we would like to test accuracy of HWENO scheme when it apply to solve the equation (4.1) with initial condition:

$$u(x, 0) = \sin(\pi x), \tag{4.2}$$

and periodic boundary condition. We compute the solution up to $t = 2$, i.e., after one time period. In Table 1 the L_1, L_∞ errors and the numerical orders by HWENO and WENO schemes are shown, respectively. One can see that both the fifth-order HWENO and WENO schemes achieve their designed order of accuracy. We can also see that errors by HWENO are smaller than those by WENO under the same number grid points.

Table 1 Linear equation

N	HWENO5				WENO5			
	L_1 error	Order	L_∞ error	Order	L_1 error	Order	L_∞ error	Order
10	1.79E-03		3.10E−03		3.82E−03		6.66E−03	
20	5.52E−05	5.02	1.00E−04	4.95	1.50E−04	4.67	2.95E−04	4.50
40	1.49E−06	5.21	2.97E−06	5.08	4.21E−06	5.16	8.81E−06	5.07
80	4.52E−08	5.04	9.28E−08	5.00	1.25E−07	5.07	2.75E−07	5.00
160	1.40E−09	5.02	2.80E−09	5.05	3.86E−09	5.02	8.25E−09	5.06
320	4.33E−11	5.01	7.87E−11	5.15	1.19E−10	5.01	2.36E−10	5.13
640	1.34E−12	5.01	2.34E−12	5.08	3.70E−12	5.01	6.56E−12	5.17

L^1 and L^∞ errors and numerical order of accuracy

Next, we test Eq. (4.1) with initial condition which is discontinuous to show resolution of HWENO schemes. The initial condition is consisting of a Gaussian, a square pulse, a sharp triangle, and a combination of semi-ellipses, given by

$$u(x,0) = \begin{cases} \frac{1}{6}[G(x, \beta, z - \delta) + 4G(x, \beta, z) + G(x, \beta, z + \delta)], & -0.8 \le x \le -0.6, \\ 1, & -0.4 \le x \le -0.2, \\ 1 - |10(x - 0.1)|, & 0 \le x \le 0.2, \\ \frac{1}{6}[F(x, \beta, a - \delta) + 4F(x, \beta, a) + F(x, \beta, a + \delta)], & 0.4 \le x \le 0.6, \\ 0, & \text{otherwise,} \end{cases} \quad (4.3)$$

$$G(x, \beta, z) = e^{-\beta(x-z)^2}, \quad F(x, \alpha, a) = \sqrt{\max(1 - \alpha^2(x - a)^2, 0)},$$

where the constants are $a = 0.5$, $z = -0.7$, $\delta = 0.005$, $\alpha = 10$ and $\beta = \frac{\log 2}{36\delta^2}$. We solve the problem on a 100 element uniform mesh with periodic boundary conditions and the results of HWENO are compared against the classic WENO until the final time $t = 8$, shown in Fig. 1. The solid line is the exact solution. We observe that the solution is better resolved. There is a good agreement between the exact and computed solution by HWENO. We also note that the HWENO behaves quantitatively equivalent to WENO schemes.

Example 4.2 Convex $f(u)$ with smooth initial data. In this example we test our scheme on the nonlinear Burgers' equation

$$\begin{cases} u_t + (u^2/2)_x = 0, \\ u(x, 0) = 0.5 + \sin(\pi x) \end{cases} \quad (4.4)$$

with a 2-periodic boundary conditions.

When $t = 0.5/\pi$ the solution is still smooth, and the numerical errors and accuracy orders by the HWENO5 methods and WENO5 methods are shown in Table 2. We can see that the HWENO5 schemes achieve its designed accuracy order. Comparing with the WENO5 schemes, the errors generated by HWENO5 are smaller than WENO5 schemes under the same grids, and the accuracy orders are higher than WENO5 schemes. In Fig. 2 we show the solution with $N = 80$ at the final time $t = 1.5/\pi$ compared against the classic WENO5 schemes. We observe that the HWENO5 schemes and WENO5 schemes have similar resolution for this test case.
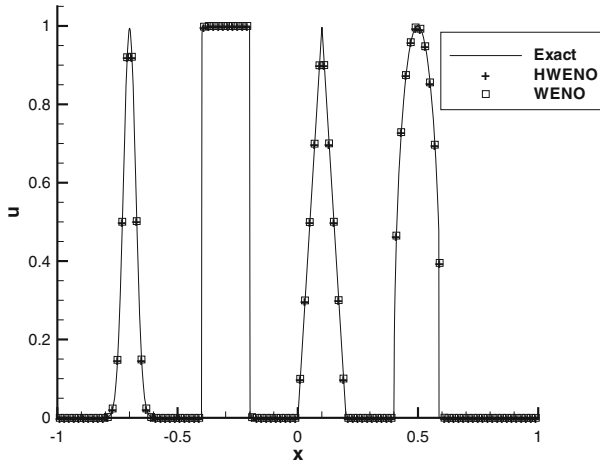
Fig. 1 Numerical solution of the linear advection equation with the discontinuous initial condition (4.3) as computed by the HWENO and WENO with $N = 100$ at $t = 8$. *Solid line* exact solution, *plus signs* HWENO, *square signs* WENO

Table 2 Burgers' equation

N	HWENO5				WENO5			
	L_1 error	Order	L_∞ error	Order	L_1 error	Order	L_∞ error	Order
10	3.21E−02		6.71E−02		1.91E−02		7.47E−02	
20	2.51E−03	3.68	7.98E−03	3.07	2.07E−03	3.21	1.21E−02	2.62
40	1.05E−04	4.58	4.82E−04	4.05	1.32E−04	3.97	1.04E−03	3.54
80	3.36E−06	4.96	1.68E−05	4.84	4.61E−06	4.84	4.73E−05	4.46
160	1.22E−07	4.78	6.53E−07	4.69	1.79E−07	4.69	1.50E−06	4.98
320	3.48E−09	5.13	3.20E−08	4.35	6.90E−09	4.70	1.37E−07	3.45
640	7.90E−11	5.46	4.42E−10	6.18	2.02E−10	5.09	7.63E−09	4.17

L^1 and L^∞ errors and numerical order of accuracy are measured at the center of each element. Using N equally spaced cells

Example 4.3 Riemann initial value problem (IVP) for nonconvex $f(u)$ [2]. We solve the nonlinear nonconvex Riemann IVP

$$u_t + \tfrac{1}{4}(u^2 - 1)(u^2 - 4) = 0,$$
$$u(x, 0) = \begin{cases} u_L & x < 0, \\ u_R & x > 0, \end{cases} \tag{4.5}$$

with two different initial Riemann conditions.

Case (i). $u_L = 2$, $u_R = -2$. The exact solution in this case is

$$u(x, t) = \begin{cases} 2, & x/t < -0.5281529, \\ f'^{-1}(x/t), & |x|/t < 0.5281529, \\ -2, & x/t > 0.5281529. \end{cases} \tag{4.6}$$
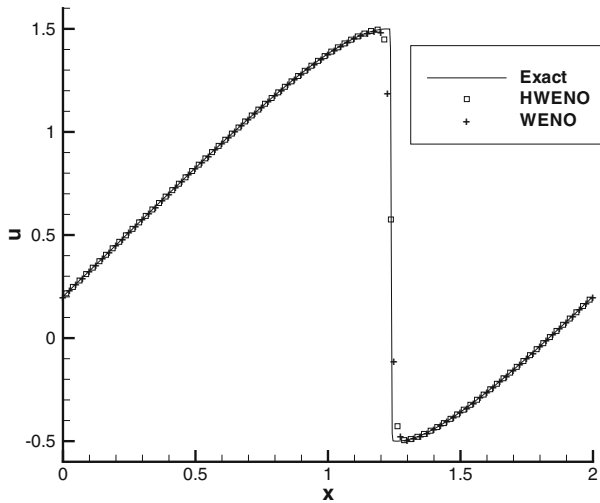
Fig. 2 Numerical solution of the Burgers' equation as computed by the HWENO and WENO with $N = 80$ at $t = 1.5/\pi$
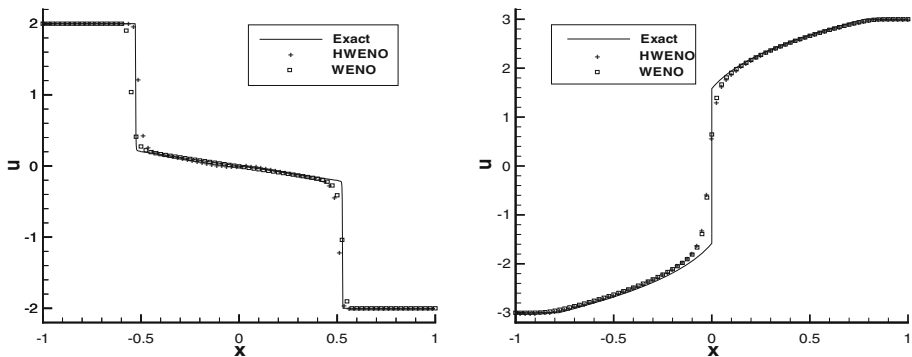

Fig. 3 Numerical solution of the nonlinear nonconvex problem with the Riemann initial condition as computed by the HWENO and WENO with $N = 80$. *Left* for case (**i**); *right* for case (**ii**)

Case (ii). $u_L = -3$, $u_R = 3$. The exact solution in this case is

$$u(x, t) = \begin{cases} -3, & x/t < -19.5, \\ f'^{-1}(x/t), & -19.5 \leq x/t \leq 0, \\ -f'^{-1}(-x/t), & 0 \leq x/t \leq 19.5, \\ 3, & x/t \geq 19.5. \end{cases} \tag{4.7}$$

In Fig. 3, we show the results of the HWENO schemes for these two cases compared to the WENO schemes. We observe that the location of the computed shocks is accurate in these two calculations. Although we observe that the computed shocks ahead of the correct location or lags behind the correct location, we find that the quality of the numerical approximation in both schemes is similar.

Table 3 The Euler equation

N	HWENO5				WENO5			
	L_1 error	Order	L_∞ error	Order	L_1 error	Order	L_∞ error	Order
10	3.38E−03		5.18E−03		3.82E−03		6.66E−03	
20	1.28E−04	4.72	2.43E−04	4.41	1.50E−04	4.67	2.95E−04	4.50
40	3.77E−06	5.09	7.25E−06	5.07	4.21E−06	5.16	8.81E−06	5.07
80	1.15E−07	5.04	2.22E−07	5.03	1.25E−07	5.07	2.75E−07	5.00
160	3.49E−09	5.04	6.31E−09	5.14	3.86E−09	5.02	8.25E−09	5.06
320	1.05E−10	5.06	1.79E−10	5.14	1.19E−10	5.01	2.36E−10	5.13

L^1 and L^∞ errors and numerical order of accuracy are measured at the center of each element. Using N equally spaced cells

4.2 Euler System of Gas Dynamics in One Dimension

In this subsection, we present numerical experiments with the one dimensional system of the Euler equations for gas dynamics in conservation form:

$$
\begin{pmatrix} \rho \\ \rho u \\ E \end{pmatrix}_t + \begin{pmatrix} \rho u \\ \rho u^2 + p \\ u(E + p) \end{pmatrix}_x = 0, \tag{4.8}
$$

here ρ is the density, u is the velocity, E is the total energy, p is the pressure, which is related to the total energy by $E = \frac{p}{\gamma-1} + \frac{1}{2}\rho u^2$ with $\gamma = 1.4$.

Example 4.4 Accuracy tests. We solve the nonlinear system of Euler equations. The domain we take $[-1, 1]$, the initial condition is set to be $\rho(x, t) = 1 + 0.2\sin(\pi x)$, $v(x, 0) = 1$, $p(x, 0) = 1$. Periodic boundary condition are used for original Euler equations and its derivative equations. The exact solution is $\rho(x, t) = 1 + 0.2\sin(\pi(x - t))$, $v(x, t) = 1$, $p(x, t) = 1$.

We present errors in the L^1 and L^∞ norm and theirs numerical orders of accuracy of the density ρ at $t = 2$ on uniform meshes having 10, 20, 40, 80, 160, and 320 elements for the HWENO schemes in Table 3, in comparison with the results of classical WENO methods [5,10] for this numerical example. Obviously, the HWENO schemes achieve their designed fifth order accuracy. We observe that the errors of the WENO scheme are significantly bigger than those for the schemes designed in this paper in Table 3.

Following we consider here three well known Riemann problems involving very strong discontinuities problems.

Example 4.5 Riemann initial value problems: Lax and Sod's problem. Here we show that the HWENO scheme passes the test of the Riemann initial value problems, also known as the Lax problem and Sod's problem. The numerical experiments were conducted using 200 grid points. For the Lax problems, the density ρ, velocity u and pressure p in the left and the right stages of the shock are:

$$
(\rho, v, p) = \begin{cases} (0.445, 0.698, 3.528) & \text{if } x \le 0, \\ (0.5, 0, 0.571) & \text{if } x > 0, \end{cases}
$$

and the Sod's problem,

$$
(\rho, v, p) = \begin{cases} (1, 0, 1) & \text{if } x \le 0, \\ (0.125, 0, 0.1) & \text{if } x > 0, \end{cases}
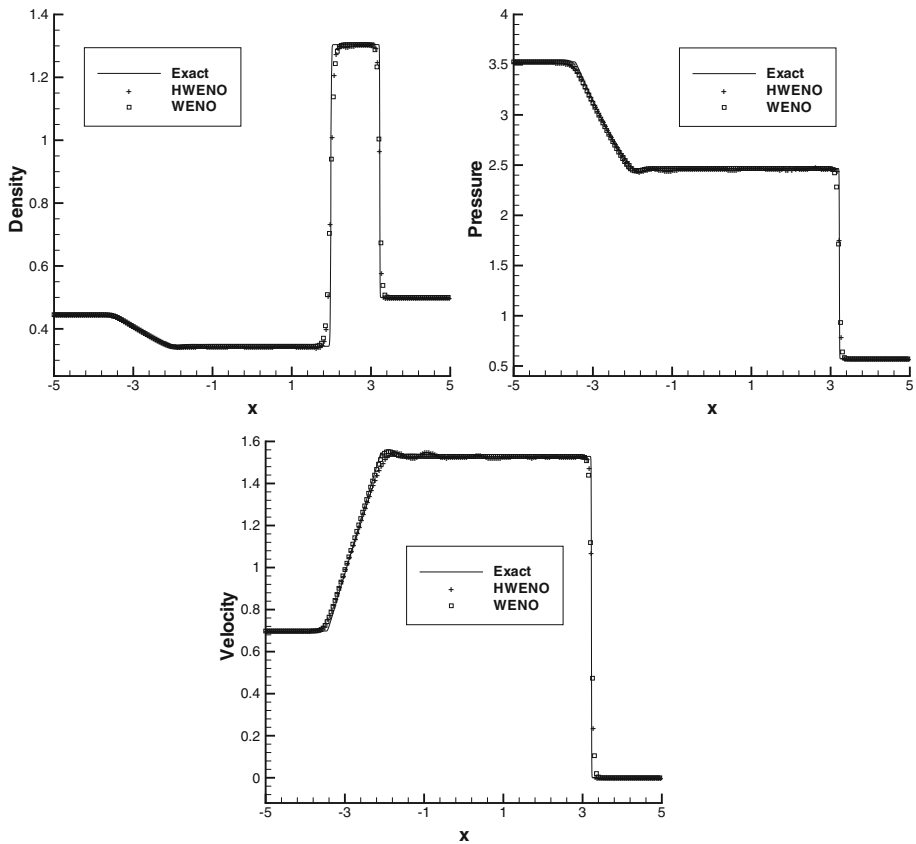$$

Fig. 4 Numerical solution of the Lax problem with the Riemann initial condition as computed by the HWENO and WENO with $N = 200$

and the final time is $t = 1.3$ (for Lax problem) and $t = 2$ (for Sod's problem) for both problems separately. The computational domain is $[-5, 5]$. We use the constant boundaries for equations and its derivative equations. The numerical results (symbols) of density, pressure and velocity are shown along with the exact solutions (solid black lines).

The numerical results are presented in Figs. 4 and 5. We note that figures are the comparable HWENO schemes with classical WENO schemes. We can see that this paper's schemes give the correct solution with good resolution. The improvement in the resolution of shock waves is more apparent from figures. We observe also that the numerical results for our schemes keep sharp transition, but according to our experience with expensive numerical testing, for this scheme, especially for the Lax problem, it is tough and the oscillations can easily appear. Here the classical WENO scheme performs better than our schemes, although it gives basic correct conclusions as the exact solution.

Example 4.6 The shock density wave interaction problem [11]. The solution of this problem contains both shocks and complex smooth regions, i.e. solving the Euler equation with a moving Mach=3 shock interacting with the sine waves in density, specified by the following initial conditions:
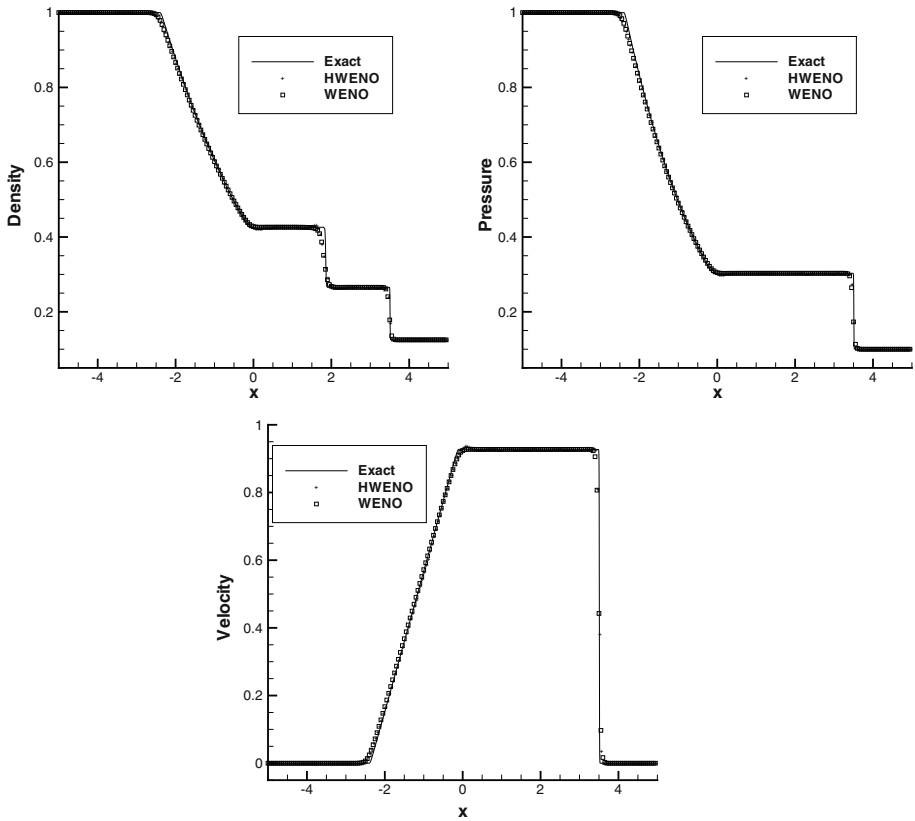
Fig. 5 Numerical solution of the sod's problem with the Riemann initial condition as computed by the HWENO and WENO with $N = 200$

$$(\rho, v, p) = \begin{cases} (3.857143, 2.629369, 10.333333) & \text{if } x < -4, \\ (1 + \varepsilon \sin(5x), 0, 1) & \text{if } x \geq -4. \end{cases}$$

In our test, we take $\varepsilon = 0.2$. The computational domain is $x \in [-5, 5]$. The solution of this problem consists of a number of shocklets and fine scales structures which are located behind a right-going mains hock. Generally for the shock or disconnect problems, our key concern is resolution and sharp transition of the solution, but the accuracy of schemes is not so important. The goal of this test is to show the advantage of HWENO schemes that is a higher order scheme, when the solution contains both shock and complex smooth region structures.

We take the periodic boundary conditions for this problem. In Fig. 6, we provide a comparison of the density, pressure and velocity for HWENO and WENO schemes at $t = 1.8$ with $N = 300$ against the reference solutions, which is a converged solution computed by fifth order finite difference WENO method with 2,000 grid points. We can see that HWENO schemes converge properly to reference solution and capture fine scale structure of the solution, particularly at the high-frequency waves behind the shock. And comparing with the WENO scheme, HWENO schemes have better sharp transition or resolution.
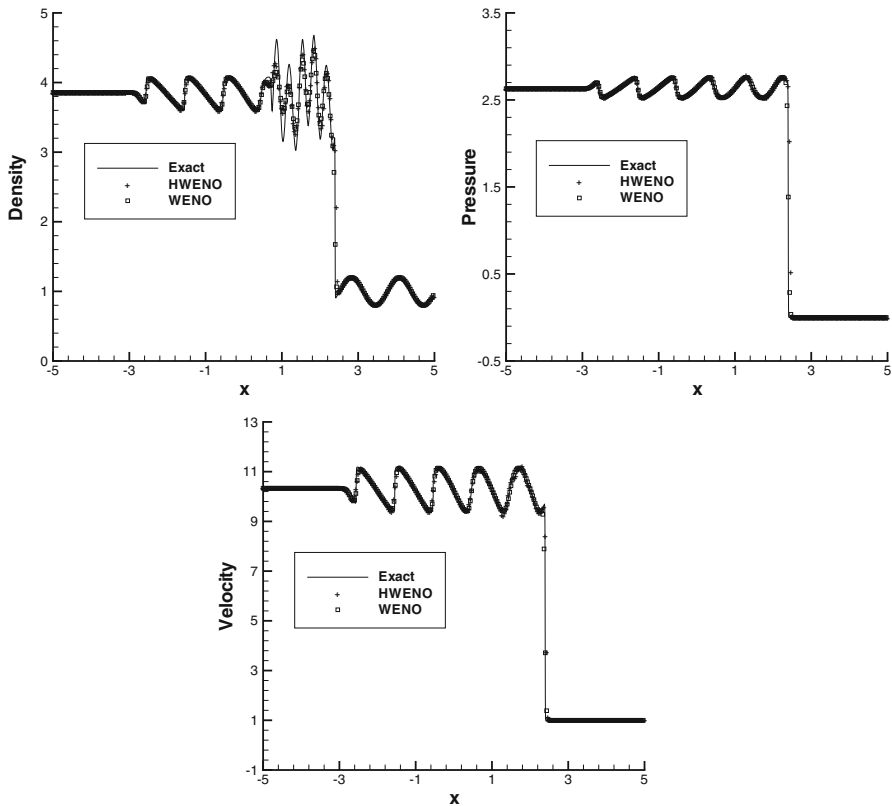
Fig. 6 Numerical solution of the Shu–Osher problem with the Riemann initial condition as computed by the HWENO and WENO with $N = 300$

4.3 Scalar Conservation Laws in Two Dimensions

Example 4.7 The two dimensional linear advection problem. We consider the two dimensional linear advection equation:

$$\begin{cases} u_t + u_x + u_y = 0, & (x, y) \in R^2, \ t > 0, \\ u(x, y, 0) = u_0(x, y). \end{cases} \tag{4.9}$$

The exact solution of this problem is $u(x, y, t) = u_0(x - t, y - t)$. We would like to test accuracy of HWENO scheme when it apply to solve the equation (4.9) with initial condition:

$$u(x, \ y, \ 0) = 0.5 + \sin(\pi(x + y)), \tag{4.10}$$

and periodic boundary condition. We compute the solution up to $t = 1$. In Table 4 the L_1, L_2 and L_∞ errors and the numerical orders by HWENO scheme are shown, respectively. We can see that the fourth-order HWENO scheme achieves its designed order of accuracy.

Example 4.8 Burgers' equation. We solve the two-dimensional nonlinear Burgers' equation $u_t + (u^2/2)_x + (u^2/2)_y = 0, 0 \le x \le 4, u(x, y, 0) = u_0(x, y)$, with periodic boundary conditions. Here we consider the hyperbolic conservation laws on test problems with exact solution case. The initial condition is $u_0(x + y) = 0.5 + \sin((x + y)\pi/2)$. We list the L_1

Table 4 Fourth order HWENO spatial discretization scheme, for the two dimensional linear equation with initial condition $u_0(x) = 0.5 + \sin(\pi(x + y))$, $t = 1$

$Nx \times Ny$	L_1 error	Order	L_2 error	Order	L_∞ error	Order
10 * 10	3.70E−01		4.08E−01		5.61E−01	
20 * 20	7.52E−02	2.30	8.98E−02	2.19	1.59E−01	1.82
40 * 40	1.89E−02	1.99	2.19E−02	2.03	4.19E−02	1.92
80 * 80	5.07E−03	1.90	6.39E−03	1.78	1.31E−02	1.67
160 * 160	1.06E−04	5.58	1.74E−04	5.20	5.34E−04	4.62
320 * 320	7.18E−07	7.21	1.06E−06	7.36	2.84E−06	7.55
640 * 640	1.09E−08	6.04	1.43E−08	6.22	3.23E−08	6.46

Table 5 Fourth order HWENO spatial discretization scheme, for the two dimensional Burgers' equation $u_t + (u^2/2)_x + (u^2/2)_y = 0$ with initial condition $u_0(x) = 0.5 + \sin((x + y)\pi/2)$, $t = 0.5/\pi$

$Nx \times Ny$	L_1 error	Order	L_2 error	Order	L_∞ error	Order
10 * 10	6.41E−02		5.89E−02		6.94E−02	
20 * 20	5.47E−03	3.55	4.06E−03	3.86	6.74E−03	3.36
40 * 40	8.13E−04	2.75	5.58E−04	2.86	9.19E−04	2.87
80 * 80	1.97E−04	2.05	2.53E−04	1.14	6.23E−04	0.56
160 * 160	1.02E−05	4.27	1.69E−05	3.90	5.37E−05	3.54
320 * 320	9.28E−08	6.77	1.28E−07	7.05	4.08E−07	7.04
640 * 640	2.87E−09	5.02	2.98E−09	5.43	6.90E−09	5.89

Table 6 The two-dimensional Euler equation

$Nx \times Ny$	L_1 error	Order	L_2 error	Order	L_∞ error	Order
10*10	3.32E−02		4.03E−02		6.75E−02	
20*20	5.70E−03	2.54	7.82E−03	2.36	1.82E−02	1.89
40*40	2.43E−03	1.23	3.09E−03	1.34	7.27E−03	1.33
80*80	8.47E−06	8.17	1.16E−05	8.06	2.91E−05	7.97
160*160	1.32E−07	6.00	1.58E−07	6.20	2.84E−07	6.68
320*320	7.30E−09	4.18	8.18E−09	4.27	1.74E−08	4.03
640*640	4.52E−10	4.01	5.02E−10	4.02	7.10E−10	4.04

L^1, L^2 and L^∞ errors and numerical order of accuracy by HWENO are measured at the center of each element. Using N equally spaced cells

and L_∞ errors for the nodal value at time $t = 0.5/\pi$ in Table 5. We can see that the designed fourth order accuracy is achieved in the three norms for both of schemes.

4.4 Euler System in Two Dimensions

In this section, we apply the HWENO schemes to solve the two dimensional Euler equation, including the Riemann problem, Shock–vortex (SV) interaction, double mach reflection problem and the forward step problem. The governing equations are the two-dimensional Euler equations in Cartesian coordinates given by
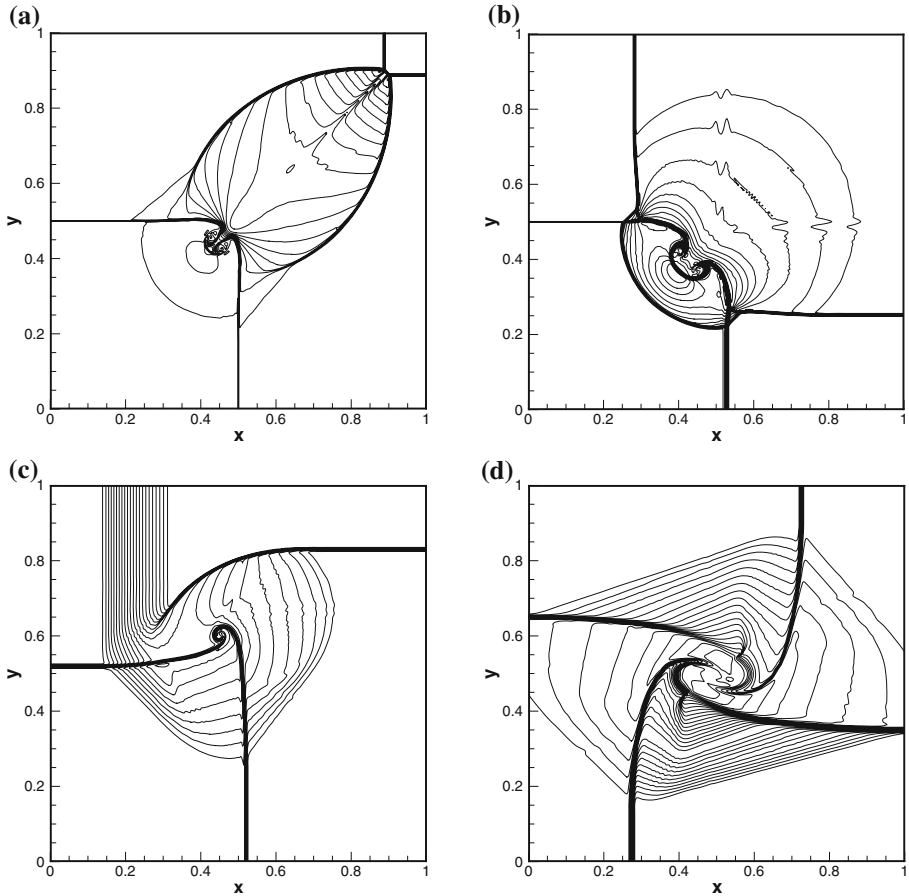
Fig. 7 Numerical solution of the four Riemann problems computed by the HWENO with $N = 400 \times 400$. 30 equally spaced density contours are *plotted*, respectively

$$\begin{pmatrix} \rho \\ \rho u \\ \rho v \\ E \end{pmatrix}_t + \begin{pmatrix} \rho u \\ \rho u^2 + p \\ \rho u v \\ u(E + p) \end{pmatrix}_x + \begin{pmatrix} \rho v \\ \rho u v \\ \rho v^2 + p \\ v(E + p) \end{pmatrix}_y = 0, \tag{4.11}$$

here ρ is the density, (u, v) is the velocity in x-dir. and y-dir., E is the total energy, p is the pressure, which is related to the total energy by $E = \frac{p}{\gamma - 1} + \frac{1}{2}\rho(u^2 + v^2)$ with $\gamma = 1.4$. The computations are carried out with a CFL number of 0.2.

Example 4.9 Accuracy test. We solve the two dimensional nonlinear systems of Euler equations (4.11). The initial condition is set to be $\rho(x, y, t) = 1 + 0.2\sin(\pi(x + y))$, $u(x, y, 0) = 0.7$, $v(x, y, 0) = 0.3$, $p(x, y, 0) = 1$. We consider this problem in the domain of $[0, 2] \times [0, 2]$. Periodic boundary condition is used for original Euler equations and its derivative equations. We compute the solution up to $t = 2$. The exact solution is $\rho(x, y, t) = 1 + 0.2\sin(\pi((x + y) - (u + v)t))$, $u(x, y, t) = 0.7$, $v(x, y, t) = 0.3$, $p(x, y, t) = 1$.
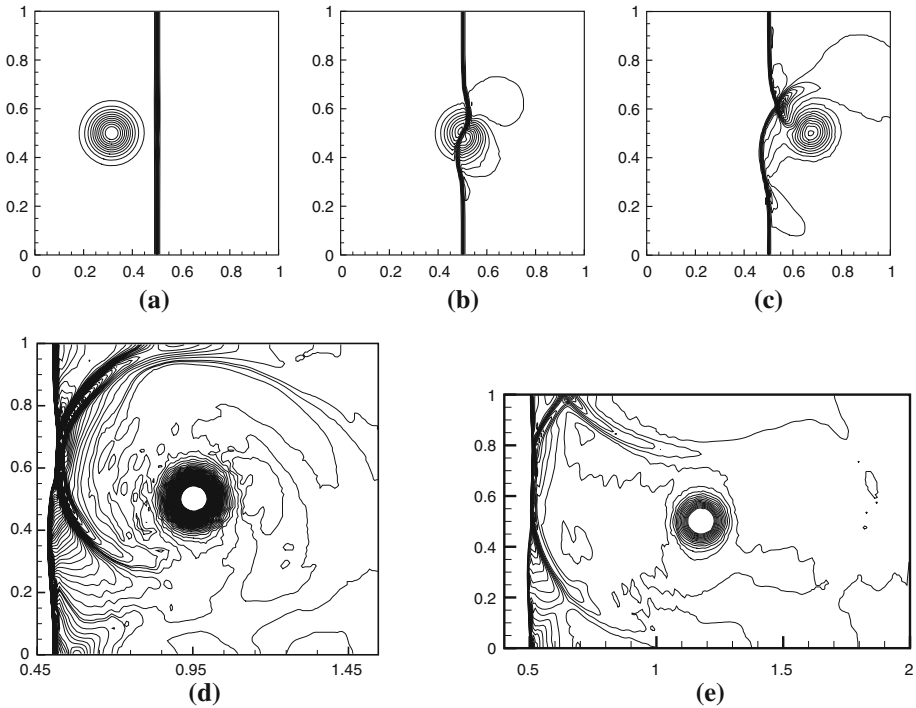
Fig. 8 2D shock vortex interaction. Pressure. 30 contours for (**a**)–(**c**) and (**e**), *d* 90 contours. **a** $t = 0.05$., **b** $t = 0.2$., **c** $t = 0.35$., **d** $t = 0.6$. **e** $t = 0.8$.

We present errors in the L^1 and L^∞ norm and theirs numerical orders of accuracy of the density ρ on uniform meshes for the HWENO scheme in Table 6. Obviously, the HWENO schemes achieve their designed order of accuracy.

Example 4.10 The Riemann problem. In this example we present numerical experiments with the HWENO schemes for four two-dimensional Riemann problems, the initial conditions are as follows, respectively:

$$
a. \ (\rho, u, v, p)^T = \begin{cases} (0.5313, 0, 0, 0.4)^T, & x > 0.5, \ y > 0.5, \\ (1, 0.7276, 0, 1)^T, & x < 0.5, \ y > 0.5, \\ (0.8, 0, 0, 1)^T, & x < 0.5, \ y < 0.5, \\ (1, 0, 0.7276, 1)^T, & x > 0.5, \ y < 0.5, \end{cases}
\tag{4.12}
$$

$$
b. \ (\rho, u, v, p)^T = \begin{cases} (1, 0.1, 0, 1)^T, & x > 0.5, \ y > 0.5, \\ (0.5313, 0.8276, 0, 0.4)^T, & x < 0.5, \ y > 0.5, \\ (0.8, 0.1, 0, 0.4)^T, & x < 0.5, \ y < 0.5, \\ (0.5313, 0.1, 0.7276, 0.4)^T, & x > 0.5, \ y < 0.5, \end{cases}
\tag{4.13}
$$

$$
c. \ (\rho, u, v, p)^T = \begin{cases} (0.5313, 0.1, 0.1, 0.4)^T, & x > 0.5, \ y > 0.5, \\ (1.0222, -0.6179, 0.1, 1)^T, & x < 0.5, \ y > 0.5, \\ (0.8, 0.1, 0.1, 1)^T, & x < 0.5, \ y < 0.5, \\ (1, 0.1, 0.8276, 1)^T, & x > 0.5, \ y < 0.5, \end{cases}
\tag{4.14}
$$

(a) 960×240 meshes
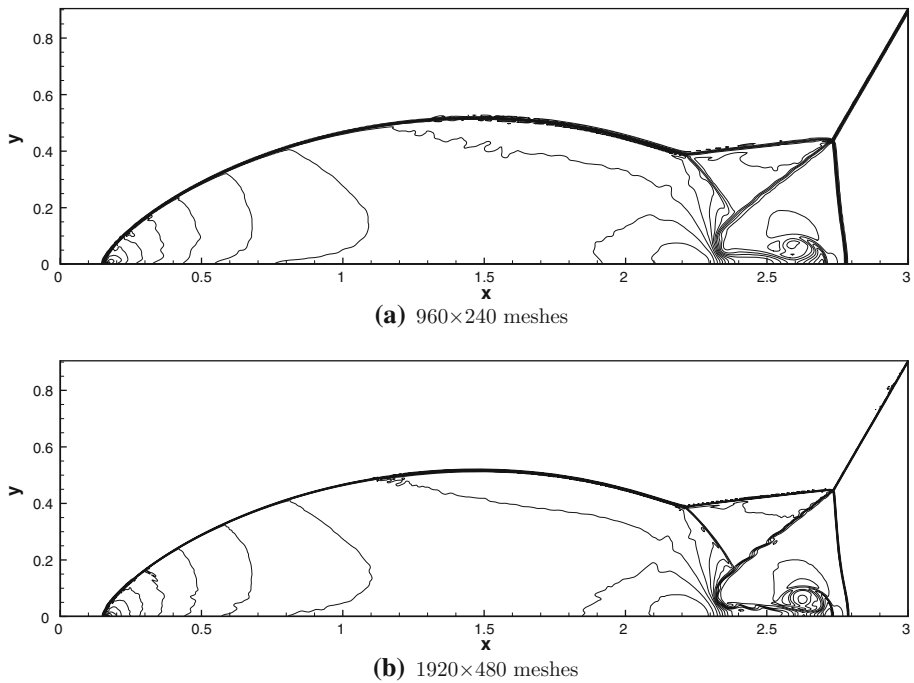

(b) 1920×480 meshes

Fig. 9 Density plot for double mach reflection

$$d. \ (\rho, u, v, p)^T = \begin{cases} (1, 0.75, -0.5, 1)^T, & x > 0.5, \ y > 0.5, \\ (2, 0.75, 0.5, 1)^T, & x < 0.5, \ y > 0.5, \\ (1, -0.75, 0.5, 1)^T, & x < 0.5, \ y < 0.5, \\ (3, -0.75, -0.5, 1)^T, & x > 0.5, \ y < 0.5. \end{cases} \tag{4.15}$$

The computational domain is taken to be $[0, 1] \times [0, 1]$, with 400×400 grid points, and the final computational times are a. $t = 0.25$, b. $t = 0.3$, c. $t = 0.2$, d.$t = 0.3$ for the four Riemann problems, respectively. In the Fig. 7 the computational densities by HWENO schemes for the Riemann problems are shown. We can observe that most of the flow features are captured well for all these Riemann problems.

Example 4.11 Shock–vortex interaction. In this test, we use the HWENO schemes to simulate the model of the interaction between a stationary shock and vortex. The computational domain is chosen to be $[0, 2] \times [0, 1]$. A stationary Mach 1.1 shock is positioned at $x = 0.5$ and normal to the x-axis. A uniform mesh of 251×100 in the computational domain is used. There is a small vortex at the flow left to the shock, its center is $(x_c, y_c) = (0.25, 0.5)$. The initial left state is $(\rho, u, v, p) = (1, 1.1\sqrt{\gamma}, 0, 1)$. Its right state can be easily make sure by the *Rankine − Hugoniot* condition. The problem is initialized by the vortex as a perturbation to the velocity (u, v), temperature $(T = p/\rho)$, and entropy $(S = \ln(p/\rho^\gamma))$ of the mean flow and we can denote them by the following values:

$$u' = \varepsilon \tau e^{\alpha(1-\tau^2)} \sin\theta,$$
$$v' = -\varepsilon \tau e^{\alpha(1-\tau^2)} \cos\theta,$$
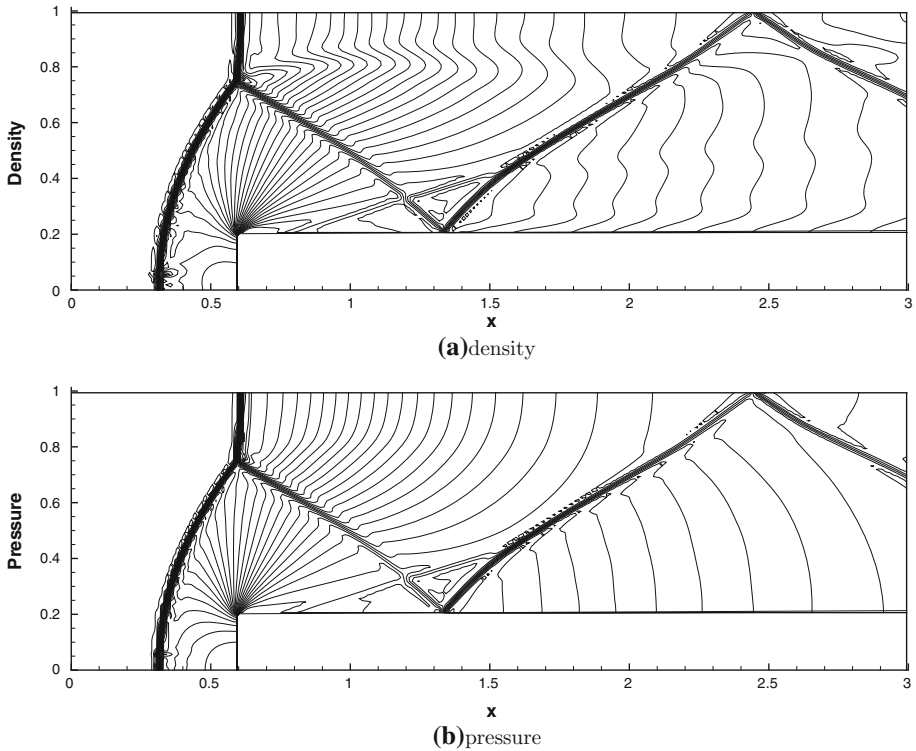
(a) density

(b) pressure

Fig. 10 Forward step problem with 240×80 cells. 30 equally spaced density and pressure contours from 0.32 to 6.3 and from 0.35 to 13, separately

$$T' = -\frac{(\gamma - 1)\varepsilon^2 e^{2\alpha(1-\tau^2)}}{4\alpha\gamma},$$

$$S' = 0,$$

where $\tau = r/r_c$, $r = \sqrt{(x-x_0)^2 + (y-y_0)^2}$, $\varepsilon = 0.3$, $r_c = 0.05$ and $\alpha = 0.204$. Note that here the ε, α and r_c indicate the strength, the decay rate and the radius (maximum strength) of the vortex. For more details, one can see [5,10]. The reflective boundary conditions are used at the upper and lower boundaries. In the SV interaction, an acoustic wave front is generated and fine scale structures are formed behind the main shock. These are well captured by HWENO schemes. The pressure contours obtained by HWENO at time $t = 0.05$, $t = 0.2$, $t = 0.35$, $t = 0.6$ and $t = 0.8$ are shown in Fig. 8. Comparing the qualitative to [5], we can see that the results show the present HWENO method can attain high accuracy order and capture the vortex and the shock very well.

Example 4.12 Double Mach reflection. This problem is originally from [13]. The computational domain for this problem is $[0, 4] \times [0, 1]$. The reflecting wall lies at the bottom, starting from $x = \frac{1}{6}$. Initially a right-moving Mach 10 shock is positioned at $x = \frac{1}{6}$, $y = 0$ and makes a $60°$ angle with the x-axis. For the bottom boundary, the exact post-shock condition is imposed for the part from $x = 0$ to $x = \frac{1}{6}$ and a reflective boundary condition is used for the rest. At the top boundary, the flow values are set to describe the exact motion of a Mach 10 shock. Free stream inflow and out flow boundary conditions are imposed in the inflow and

the out flow boundaries. We compute the solution up to $t = 0.2$. 30 equally spaced density contours from 0.9 to 22.6, with two different uniform meshes 960×240 and $1,920 \times 480$, are plotted in Fig. 9.

Example 4.13 A Mach 3 *wind tunnel with a step.* This model problem is also originally from [13]. The setup of the problem is as follows. The wind tunnel is 1 length unit wide and 3 length units long. The step is 0.2 length units high and is located 0.6 length units from the left-hand end of the tunnel. The problem is initialized by a right-going Mach 3 flow. Reflective boundary conditions are applied along the wall of the tunnel and in/out flow boundary conditions are applied at the entrance/exit. The corner of the step is a singular point and we treat it the same way as in [13], which is based on the assumption of a nearly steady flow in the region near the corner. The density is plotted at $t = 4.0$ are given in Fig. 10 with 30 equally spaced density contours from 0.32 to 6.3, pressure contours from 0.35 to 13.

5 Concluding Remarks

In 2004, the HWENO method was developed by Qiu and Shu [7, 8], in which the construction of HWENO schemes was based on a finite volume formulation. In this paper, we presented another version of scheme, finite difference HWENO method. Finite difference formulation have proved to be more computationally efficient than the finite volume formulation to the high accuracy order schemes when they are applied to multi-dimensional cases. One major advantage of HWENO schemes is its compactness in the reconstruction. For example, five points are needed in the stencil for a fifth order WENO reconstruction, while only three points are needed for a fifth order HWENO (HWENO5) reconstruction. The numerical errors by HWENO5 are smaller than WENO5 schemes under the same grids in our test cases. But we would also like to point out that HWENO scheme requires about double computer memory and CPU time comparing with the original WENO scheme when using the same number of grid points, this is a weak point of HWENO comparing with the original WENO scheme.

References

1. Harten, A.: High resolution schemes for hyperbolic conservation laws. J. Comput. Phys. **49**, 357–393 (1983)
2. Harten, A., Engquist, B., Osher, S., Chakravarthy, S.R.: Uniformly high order accurate essentially non-oscillatory schemes, III. J. Comput. Phys. **71**, 231–303 (1987)
3. Harten, A., Osher, S.: Uniformly high-order accurate non-oscillatory schemes I. SIAM J. Numer. Anal. **24**, 279–309 (1987)
4. Hu, X.Y., Adams, N.A., Shu, C.-W.: Positivity-preserving method for high-order conservative schemes solving compressible Euler equations. J. Comput. Phys. **242**, 169–180 (2013)
5. Jiang, G., Shu, C.-W.: Efficient implementation of weighted ENO schemes. J. Comput. Phys. **126**, 202–228 (1996)
6. Liu, X.D., Osher, S., Chan, T.: Weighted essentially non-oscillatory schemes. J. Comput. Phys. **115**, 200–212 (1994)
7. Qiu, J., Shu, C.-W.: Hermite WENO schemes and their application as limiters for Runge–Kutta Galerkin method: one-dimension case. J. Comput. Phys. **193**, 115–135 (2004)
8. Qiu, J., Shu, C.-W.: Hermite WENO schemes and their application as limiters for Runge–Kutta discontinuous Galerkin method II: two-dimensional case. Comput. Fluids **34**, 642–663 (2005)
9. Qiu, J., Shu, C.-W.: Hermite WENO schemes for Hamilton–Jacobi equations. J. Comput. Phys. **204**, 82–99 (2005)
10. Shu, C.-W.: High order weighted essentially nonoscillatory schemes for convection dominated problems. SIAM Rev. **51**, 82–126 (2009)
11. Shu, C.-W., Osher, S.: Efficient implementation of essentially non-oscillatory shock-capturing schemes. J. Comput. Phys. **77**, 439–471 (1988)

12. Shu, C.-W., Osher, S.: Efficient implementation of essentially non-oscillatory shock-capturing schemes, II. J. Comput. Phys. **83**, 32–78 (1989)
13. Woodward, P., Colella, P.: The numerical simulation of two-dimensional fluid flow with strong shocks. J. Comput. Phys. **54**, 115–173 (1984)
14. Zhang, X., Shu, C.-W.: Maximum-principle-satisfying and positivity-preserving high-order schemes for conservation laws: survey and new developments. Proc. R. Soc. A Math. Phys. Eng. Sci. **467**, 2752–2776 (2011)
15. Zhang, X., Shu, C.-W.: Positivity-preserving high order finite difference WENO schemes for compressible Euler equations. J. Comput. Phys. **231**, 2245–2258 (2012)
16. Zhu, J., Qiu, J.: A class of the fourth order finite volume Hermite weighted essentially non-oscillatory schemes. Sci. China Ser. A Math. **51**, 1549–1560 (2008)